

# PDMD: Potential-free Data-driven Molecular Dynamics for Variable-sized Water Clusters $(\text{H}_2\text{O})_n \leq 21$

Hongyu Yan<sup>1</sup>, Qi Dai<sup>2</sup>, Yong Wei<sup>3\*</sup>, Minghan Chen<sup>4\*</sup>, and Hanning Chen<sup>5\*</sup>

<sup>1</sup>School of Engineering and Physical Sciences, Heriot-Watt University, Edinburgh EH14 4AS, UK

<sup>2</sup>Department of Computer Science, Wake Forest University, Winston-Salem, North Carolina 27104, USA

<sup>3</sup>Department of Computer Science and Information Systems, University of North Georgia, Dahlonega, Georgia 30533, USA

<sup>4</sup>Department of Computer Science, Wake Forest University, Winston-Salem, North Carolina 27104, USA

<sup>5</sup>Texas Advanced Computing Center, The University of Texas at Austin, Austin, Texas 78758, USA

\*Corresponding authors

## Abstract

Conventional molecular dynamics (MD) simulation approaches, such as *ab initio* MD and empirical force field MD, face significant trade-offs between physical accuracy and computational efficiency. This work presents a novel Potential-free Data-driven Molecular Dynamics (PDMD) framework for predicting system energy and atomic forces of variable-sized water clusters  $(\text{H}_2\text{O})_n \leq 21$ . Specifically, PDMD employs the smooth overlap of atomic positions descriptor to generate high-dimensional, equivariant features before leveraging ChemGNN, a graph neural network model that adaptively learns the atomic chemical environments without requiring a priori knowledge. Through an iterative self-consistent training approach, the converged PDMD achieves a mean absolute error of 7.1 meV/atom for energy and 59.8 meV/Å for forces, outperforming the state-of-the-art DeepMD by  $\sim 80\%$  in energy accuracy and  $\sim 200\%$  in force prediction. As a result, PDMD can reproduce the *ab initio* MD properties of water clusters at a tiny fraction of its computational cost. These results demonstrate that the proposed PDMD offers multiple-phase predictive power, enabling ultra-fast, general-purpose MD simulations while retaining *ab initio* accuracy.

# Introduction

Molecular dynamics (MD)<sup>1</sup> is one of the most popular numerical techniques for simulating temporal and spatial evolution of chemical and biological systems.<sup>2</sup> The quality of an MD simulation rests on the accuracy of its system energy,  $E$ , and atomic forces,  $\{\vec{F}_i\}_{i=1\dots N_{atom}}$ , typically evaluated as a function of atom types and atomic coordinates,<sup>3</sup> possibly in addition to bonding topology<sup>4</sup> and atomic polarizability.<sup>5</sup> For instance, in an *ab initio* MD (AIMD) simulation,<sup>6</sup>  $E$  is obtained by diagonalizing a quantum Hamiltonian matrix<sup>7</sup> while  $\{\vec{F}_i\}$  is given by the Hellmann-Feynman theorem.<sup>8</sup> In general, AIMD simulations are computationally demanding as the time to resolve many-body electron wavefunction,  $\Psi$ , proliferates over electronic degrees of freedom,  $N_{elec}$ . Even under the mean-field approximation for single-particle orbitals such as in density functional theory (DFT),<sup>9</sup> AIMD’s computational complexity is proportional to  $N_{elec}^3$ , limiting its application to large-scale systems.

A numerically efficient alternative to AIMD is the empirical force field MD (EFFMD),<sup>10</sup> wherein  $E$  is expressed as the sum of many-body bonded energies and pairwise nonbonded potentials for a given bonding topology. In modern empirical force fields (EFFs), such as CHARMM,<sup>11</sup> AMBER,<sup>12</sup> GROMAS,<sup>13</sup> and OPLS,<sup>14</sup> the bonded energies up to four-body are included to reflect bond stretching, angle bending, and dihedral torsion. By contrast, the nonbonded potentials consist of Coulomb coupling and van der Waals (vdW) forces, which can be supplemented by electric polarization to explicitly account for dispersion and induction effects such as in AMEOPA.<sup>15</sup> Usually, EFFs are parameterized against quantum potential energy surfaces (PES)<sup>16</sup> and/or experimental data<sup>17</sup> at equilibrium states, making them unsuitable for systems that are far from equilibrium. For example, the bonded stretching potential,  $E_b$ , between two atoms commonly adopts a shifted quadratic function centered at their equilibrium bond length,  $r_0$ , i.e.,  $E_b = \frac{1}{2}k(r - r_0)^2$ . This harmonic approximation is mostly reasonable for the small oscillations of a chemical bond, whereas it becomes invalid upon bond dissociation due to the increasing anharmonicity of PES. Aiming to remediate the oversimplified inter-atomic potentials in conventional EFFs, reactive force fields (RFF) such as ReaxFF<sup>18</sup> and MS-EVB<sup>19</sup> were developed to allow for more flexible potential functions and more dynamical bonding topology, enabling the simulations of chemical reactions. Nevertheless, a fully-fledged RFF demands an exhaustive exploration of the parameter space to fully reproduce a quantum PES, the majority of which

is often unknown for condensed-phase systems. Moreover, the escalated complexity of RFF significantly increases its computer execution time compared to EFF, drastically negating its intended benefits over AIMD in numerical efficiency. As a result, a novel approach to attain  $E$  and  $\{\vec{F}_i\}$  with AIMD’s level of accuracy but at the cost of EFF is highly desired.

Over the past decade, artificial intelligence (AI)<sup>20</sup> has become a powerful tool for molecular simulations<sup>21</sup> thanks to the rapid advances in specialized hardware acceleration and machine learning (ML) algorithms. The greatest advantage of data-driven AI over traditional physics-based simulations is its no need for laws of physics,<sup>22</sup> which solutions are often too hard or nearly impossible to compute. For example, the exact solution of a many-electron wavefunction,  $\Psi$ , at its ground state is unavailable due to electron correlation,<sup>23</sup> which, however, can be numerically recaptured by expressing  $\Psi$  as a weighted linear combination of Slater determinants of one-electron orbitals,  $\{\phi_n\}$ , i.e.,  $\{\Phi = \sum_i c_i \det[\{\phi_n\}^i]\}$ , where the weights,  $\{c_i\}$ , are optimized by quantum Monte Carlo (QMC)<sup>24</sup> or full configuration interaction (FCI).<sup>25</sup> In theory, countless Slater determinants could be included, but ML filters such as the Fermionic Neural Network (FNN)<sup>26</sup> filter out those with high energies and thus negligible weights. Using atomic positions  $\vec{X}_i$  and atom types  $Z_i$  as inputs, the FNN makes QMC simulations feasible beyond simple models.

Machine learning has been utilized to accelerate computational simulations by reducing the computational cost of complex models. In fluid dynamics, a convolutional neural network (CNN)<sup>27</sup> has been employed to accelerate the resolution of time-dependent velocity fields by orders of magnitude without prior knowledge of the Navier-Stokes equation.<sup>28</sup> More recently, generative adversarial network (GAN)<sup>29</sup> empowered the high-resolution simulation of the universe’s evolution over its full dynamic range using only low-resolution astronomical images collected from the Hubble Space Telescope. Similarly, many efforts have been devoted to developing the machine learning force fields (MLFF),<sup>30</sup> hoping to reproduce high-quality *ab initio* PES from a minimal set of chemical descriptors such as atom types, interatomic distances, and partial charges. Unlike the conventional kernel-based methods<sup>31</sup> that map the input chemical descriptors to a higher-dimensional feature space for linear regression, MLFFs inspired by neural networks<sup>32</sup> decompose the nonlinear dependency of *ab initio* PES onto a linear combination of learnable parameters connected by nonlinear activation functions.<sup>33</sup> For example, two fully connected hidden layers, each featuring 25 nodes, accurately predicted

liquid water’s relatively weak yet physically essential vdW potential (BP-NNP)<sup>34</sup> compared to the BLPY density functional<sup>35</sup> after transforming type 2 and type 4 interatomic distance-dependent symmetry functions<sup>36</sup> into an input vector for the dense neural work. Since BP-NNP<sup>34</sup> and other DNN- or CNN-based MLFFs such as ANI<sup>37</sup> and SchNet<sup>38</sup> cannot encode bonding topology, they often fail to distinguish bonded and non-bonded interactions, which differ remarkably in strength, range, and form.

Graph neural network (GNN)<sup>39</sup> emerges as a more natural representation of chemical systems in ML. In GNN-inspired MLFFs, the atoms and bonds are represented as nodes and edges, respectively, in a graph wherein the embedding at each node is updated by its neighbors’ message functions.<sup>40</sup> For example, in the graph neural network force field (GNNFF) model,<sup>41</sup> the total force on an atom is assumedly the sum of the contributions from a fixed number of its neighboring atoms, ensuring the sparsity of the adjacency matrix for the linearity of computational cost with system size. Unfortunately, the missing capability of energy prediction in GNNFF prevents its application under all thermodynamic conditions except for microcanonical ensembles.<sup>41</sup> As an intuitive remedy, the atomistic line graph neural network-based force field (ALIGNN-FF)<sup>42</sup> adopts a composite loss function consisting of error terms for both forces and energies. However, the relatively low quality of ALIGNN-FF’s pairwise potential could artificially destabilize an otherwise well-equilibrated system if one compares its large mean absolute error of energy,  $E^{MAE}$ ,<sup>42</sup> to the small thermal fluctuation energy,  $k_bT$ , at room temperature. In a satisfactory scenario for room-temperature MD simulation,  $E^{MAE}$  is expected to be less than 30 meV/atom.

Chemical Adaptive Graph Neural Network (ChemGNN)<sup>43</sup> is a new graph neural network model meticulously designed to delve into the intricate dynamics of interatomic interactions within atoms’ local chemical environments. The model showed salient performance in predicting graphitic carbon nitride (g-C<sub>3</sub>N<sub>4</sub>) and its doped variants’ bandgaps. At the core of its architecture, initial node embeddings and edge features encode the chemical and physical attributes of atoms and their interactions, capturing the essence of their spatial arrangement. Within the framework of ChemGNN, the influence of interatomic interactions is distilled through the aggregation of messages exchanged among neighboring atoms. The model uses a set of permutation-invariant aggregation functions that effectively capture various aspects of these interactions, revealing the underlying structure of chemical systems. Aiming to discern the significance of various aggre-

gated impacts on an atom, each aggregation function is assigned a learnable weight. Consequently, node embeddings are iteratively updated based on the amalgamated messages derived from the local chemical environment of the atoms during model training. These refined node embeddings are then used to make predictions at both the node and graph levels, such as forecasting atomic forces and system energy, thus facilitating a comprehensive understanding of molecular behaviors.

The unique multiple-phase predictive power of ChemGNN can be well demonstrated on variable-sized water clusters,  $(\text{H}_2\text{O})_n$ , which witness the onset of a gas-to-liquid phase transition upon adding water molecules, one at a time.<sup>44</sup> As shown by a vibrational spectroscopic study,<sup>45</sup>  $(\text{H}_2\text{O})_{21}$  exhibits a pronounced red shift of two O-H stretching normal modes by more than  $400\text{ cm}^{-1}$ , which was not observed in any smaller water clusters. Moreover, similar to liquid water’s “fingerprint” band,<sup>46</sup>  $(\text{H}_2\text{O})_{21}$ ’s two red-shifted infrared peaks centered at  $\sim 3300\text{ cm}^{-1}$  are relatively broad, confirming it as the minimum network to fully solvate a water molecule at its center. Therefore, the  $(\text{H}_2\text{O})_{1\leq n\leq 21}$  clusters that offer a diverse set of chemical environments were chosen as our test bed to assess the performance of ChemGNN, which is the core of our potential-free data-driven molecular dynamics (PDMD) by affording  $E$  and  $\vec{F}_i$  out of  $\vec{X}_i$  and  $Z_i$ .

## Results

### a. Performance of PDMD Model on Energy and Forces Prediction

An iterative self-consistent approach, as detailed in the Methods Section, has been employed to develop a PDMD model by minimizing the difference in system energy,  $E$ , and atomic force,  $\vec{F}_i$ , for  $(\text{H}_2\text{O})_{1\leq n\leq 21}$  clusters between PDMD and DFT/PBE. As shown in Fig. 1(a), our PDMD model achieves a mean absolute error (MAE) for  $E$  at  $7.1\text{ meV/atom}$ , which is significantly smaller than  $k_bT$  at room temperature, the threshold to distinguish energy levels in defiance of thermal fluctuations. As for  $\vec{F}_i$ , a small MAE of  $59.8\text{ meV/\AA}$  was achieved, leading to a remarkable coefficient of determination,  $R^2 = 0.99$  (Fig. 1(b)). As an additional validation, we randomly generated 5,000 structures for each of the 21  $(\text{H}_2\text{O})_{1\leq n\leq 21}$  clusters by AIMD to form a total of  $262,447,500$  (i.e.,  $\frac{21\times 5000\times 4999}{2}$ ) pairs. Then, we ranked the two structures in each pair by their energies using both PDMD and DFT/PBE. It turns out that our PDMD model has a relatively

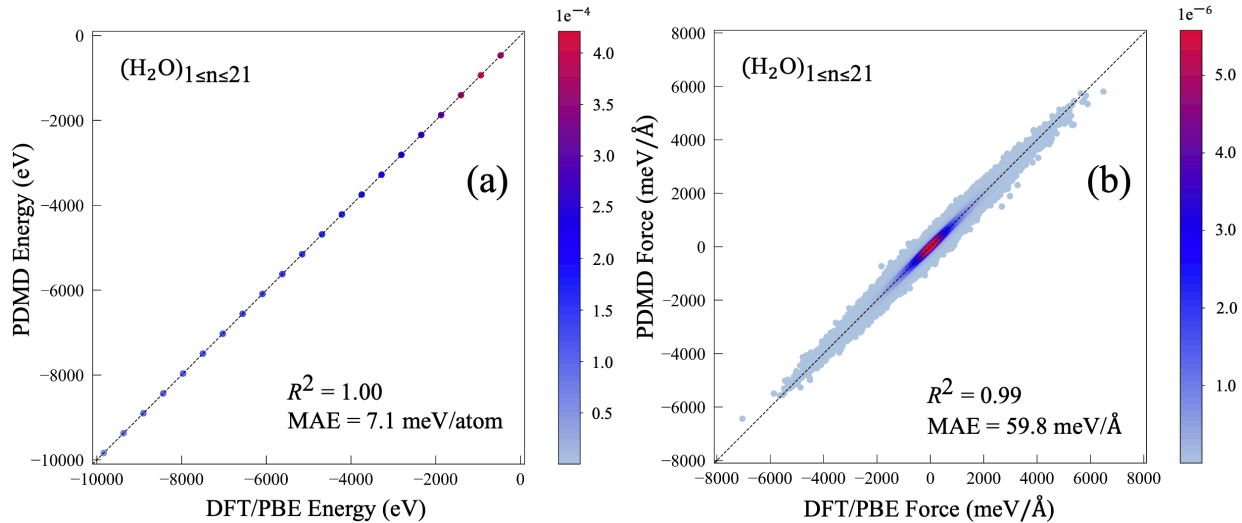


Figure 1: The mean absolute errors (MAEs) of PDMD for (a) system energy,  $E$ , and (b) atomic force,  $\vec{F}_i$ , across all  $(\text{H}_2\text{O})_{1 \leq n \leq 21}$  clusters. The data point density is reflected by color bars.

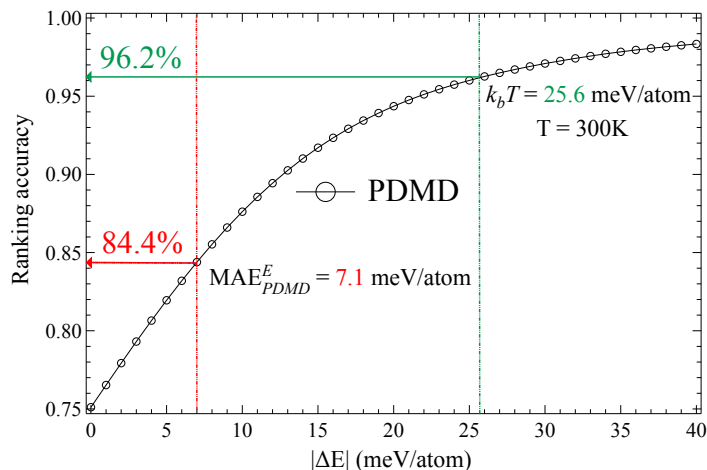


Figure 2: Ranking accuracy of PDMD model with respect to DFT/PBE for system energy.

high percentage of 84.4% to render the same rank order as DFT/PBE when the DFT/PBE energy difference,  $|\Delta E|$ , between the two structures is greater than 7.1 meV/atom (Fig. 2), the energy uncertainty of PDMD. If  $|\Delta E|$  is raised to 25.6 meV/atom (i.e.,  $k_b T$  at 300K per atom), the ranking accuracy notably increases to 96.2%, making PDMD nearly perfect for MD simulations at room temperature.

Interestingly, the MAE of  $\vec{F}_i$  obtained by PDMD is even significantly smaller than 140.0 meV/Å, the MAE between two popular DFT functionals, namely BLYP<sup>35,47</sup> and PBE<sup>48</sup> (Fig. 3), further attesting our PDMD model's quality to be on par with *ab initio* theories. A more informative assessment of PDMD is

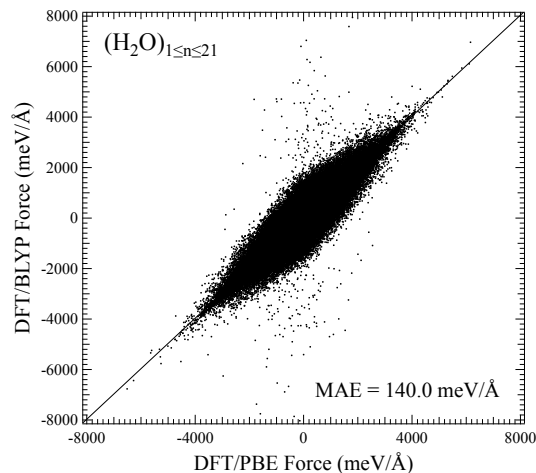


Figure 3: Comparison on atomic force,  $\vec{F}_i$ , between PBE and BLYP.

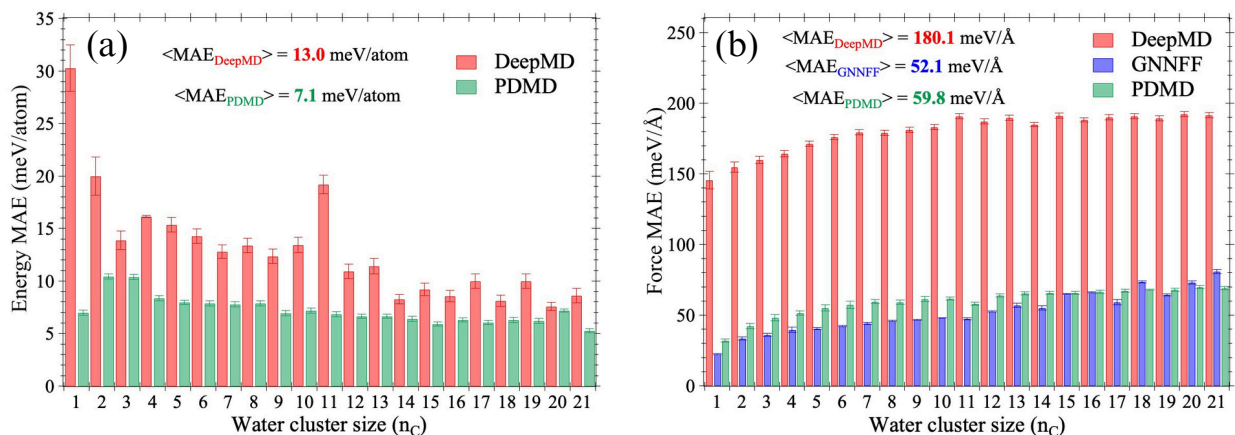


Figure 4: Performance comparison among PDMD, DeepMD, and GNNFF for (a) system energy,  $E$ , and (b) atomic force,  $\vec{F}_i$ .

to compare its performance with other molecular ML models using the same dataset. In Fig. 4(a), PDMD considerably outperforms DeepMD<sup>49</sup> by approximately 100% in energy MAE, especially for small clusters. Similarly, PDMD is superior to DeepMD<sup>49</sup> for force prediction by an even larger margin of  $\sim 200\%$  (Fig. 4(b)). In contrast, its force MAE is only 7.6 meV/Å higher than that of GNNFF,<sup>41</sup> which lacks the energy component and is thus inapplicable to MD simulations in canonical (NVT), isobaric-isothermal (NPT) and macrocanonical ( $\mu$ VT) ensembles. Taken together, our PDMD model offers a more practical data-driven solution for ultra-fast general-purpose MD simulations while retaining *ab initio* accuracy.

## b. Optimized Structures of Small Water Clusters, $(\text{H}_2\text{O})_{1 \leq n \leq 5}$

Geometry optimization of a chemical compound is driven by a finite  $\vec{F}_i$  until it vanishes and its first-order gradient (i.e., the second-order gradient of  $E$ ) remains positive. Therefore, our PDMD model is expected to afford similar optimized structures compared to DFT/PBE if it can reproduce satisfactory first-order and second-order gradients of  $E$ . Since hexamer,  $(\text{H}_2\text{O})_6$ , is the smallest water cluster that can populate multiple stable isomers at room temperature due to their nearly degenerate energy levels,<sup>50</sup> a unique optimized structure only exists for each of the five smaller water clusters, i.e.,  $(\text{H}_2\text{O})_{1 \leq n \leq 5}$ . As shown in Fig. 5, the water monomer optimized by PDMD exhibits an O-H bond length of 0.978Å, the same as that optimized by DFT/PBE. Likewise, its H-H distance of 1.523Å is only 0.003Å shorter than its DFT/PBE counterpart. Interestingly, the monomer’s distribution of O-H and H-H distances in PDMD at 300K is in excellent agreement with AIMD, demonstrating reliable bond stiffness and angular rigidity. Unlike water monomer, the optimized structures of all other clusters are stabilized by hydrogen bonds wherein a hydrogen atom covalently bonded to an oxygen atom is attracted towards another oxygen atom nearby through electrostatic interactions.<sup>51</sup> As a result, an O-H bond that participates in hydrogen bonding is slightly longer than a non-hydrogen-bonded (“dangling”) O-H bond because of partial electron transfer through the bridging hydrogen atom. This tiny yet critical bond elongation is precisely captured by both PDMD-optimized and DFT-optimized water dimers, which manifest a hydrogen-bonded O-H bond length of 0.99Å that is 0.01Å longer than its dangling counterparts (Fig. 6(a)). For maximizing their hydrogen bonds,<sup>52</sup> water trimer, tetramer, and pentamer are known to form cyclic pseudo-planar optimized structures, which PDMD legitimately generated alongside DFT in Fig. 6(b,c,d). In all these three clusters,  $(\text{H}_2\text{O})_{3 \leq n \leq 5}$ , the deviations between PDMD and DFT on hydrogen bond lengths and angles are less than 0.03Å, and 2.0°, respectively, further justifying the reliability of PDMD on modeling hydrogen bonds.

## c. Hydrogen Bonds in Large Water Clusters, $(\text{H}_2\text{O})_{6 \leq n \leq 21}$

The substantially increased variety of hydrogen bonding topology in large water clusters,  $(\text{H}_2\text{O})_{6 \leq n \leq 21}$ , allows them to adopt non-planar versatile structures featuring facile hydrogen bonds that could be easily broken and formed at room temperature. Typically, a hydrogen bond is considered to appear when the distance between



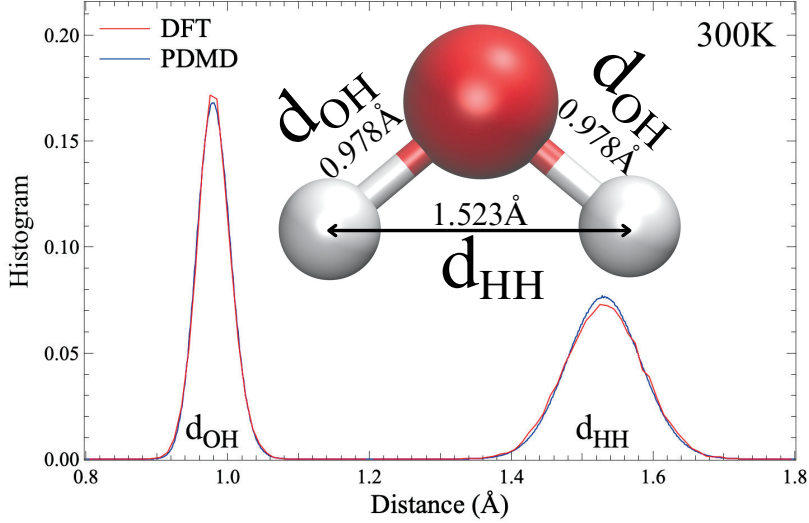
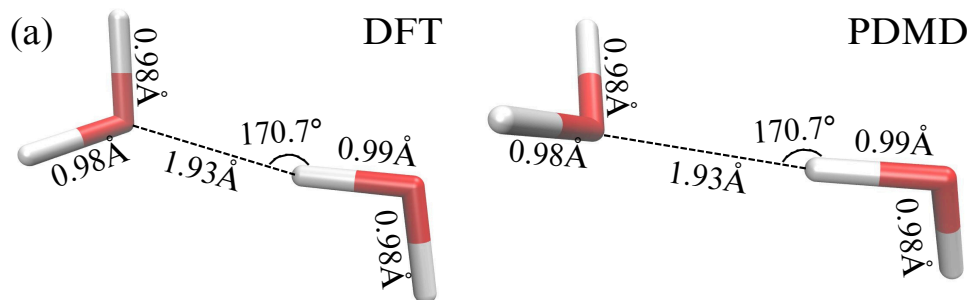
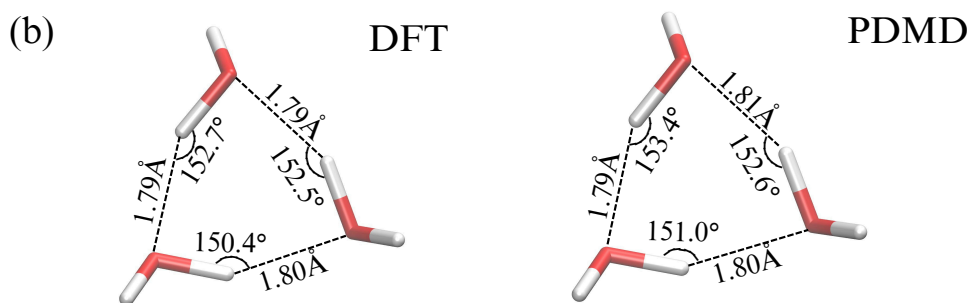


Figure 5: PDMD-optimized structure of a water monomer and its O-H and H-H distances distribution in a PDMD simulation at 300K.

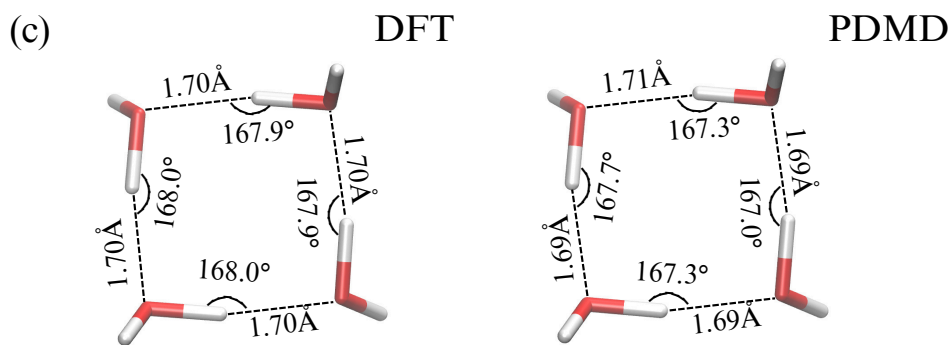
the donor and acceptor oxygen atoms is shorter than  $3.5\text{\AA}$ , and the angle between the donor, hydrogen, and acceptor atoms is greater than  $120^\circ$ . Using this criterion, the number of hydrogen bonds,  $n_{\text{HB}}$ , was calculated as a function of the cluster size,  $n_{\text{C}}$  in our PDMD trajectories. As shown in Fig. 7(a),  $n_{\text{HB}}$  grows nearly linearly at a slower pace of  $1.44n_{\text{C}}$  before  $n_{\text{C}}$  reaches 19, and after that,  $n_{\text{HB}}$  exhibits an upward bending with a much deeper slope of 2.10. Moreover, the same trend was also observed in AIMD trajectories (inset of Fig. 7(a)), albeit they are too short for quantitative reasoning. Nevertheless, this apparent acceleration of hydrogen bond formation can be ascribed to the onset of a gas-to-liquid phase transition, accompanied by a seemingly aberrant cluster shrinking for an increasing cluster size, as illustrated in Fig. 7(b). Under a pseudo-spherical approximation, the spatial dimension of a water cluster can be approximated by its radius of gyration,  $R_g$ , which is defined as  $R_g = \sqrt{\frac{\sum_{i=1}^{N_s} \sum_{j=1}^{N_a} |\vec{r}_{ij} - \vec{r}_{i0}|^2}{N_s N_a}}$ , where  $N_s$  is the number of structure snapshots,  $N_a$  is the number of atoms in a water cluster, and  $\vec{r}_{ij}$  is the coordinate of the  $j$ -th atom in the  $i$ -th snapshot, which center of mass is denoted as  $\vec{r}_{i0}$ . Although  $R_g$  persistently increases with added water molecules up to  $n_{\text{c}}=19$  as speculated, an unexpected reduction of the cluster volume occurs at  $n_{\text{c}}=20$  and  $n_{\text{c}}=21$ , wherein some water molecules start arranging tetrahedrally coordinated O-H chemical bonds and O--H hydrogen bonds for themselves for a more compact spatial pattern as always observed in liquid water. Our observation of this abnormal cluster shrinking is not only consistent with the AIMD simulations (inset of Fig. 7(b)) but



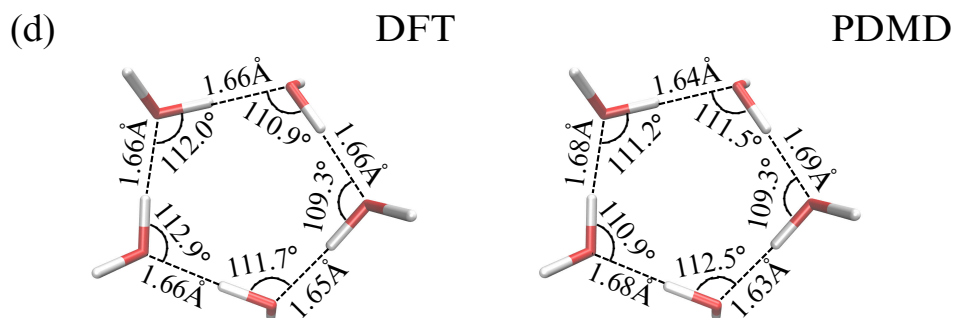
optimized structure of water dimer



optimized structure of water trimer



optimized structure of water tetramer



optimized structure of water pentamer

Figure 6: PDMD-optimized structures for water (a) dimer, (b) trimer, (c) tetramer, and (d) pentamer.

also agrees with the experimental finding that a minimum of 20 water molecules are needed to fully solvate one with two complete solvation shells evidenced by liquid water’s “fingerprint” band in  $(\text{H}_2\text{O})_{21}$ ’s infrared spectrum.<sup>45</sup> Accordingly, we also calculated the appearance probability of fully solvated water molecules in our PDMD simulations for the largest water clusters in the present study ( $(\text{H}_2\text{O})_{16 \leq n \leq 21}$ ), and found an abrupt rise when changing from  $(\text{H}_2\text{O})_{20}$  to  $(\text{H}_2\text{O})_{21}$  that once again corroborates this experimentally determined emergence of phase transition (Fig. 7(c)).

## Discussion

Over the past decade, the rapid advancement of artificial intelligence has inspired the development of machine learning molecular dynamics (MLMD),<sup>30</sup> which shows promise in greatly accelerating high-fidelity MD simulations, especially for systems with facile chemical bonds that demand accurate evaluation of system energy and atomic forces. For example, the hydrogen bond strength in water is within the kcal/mol range,<sup>53</sup> making the dynamic breaking and formation of hydrogen bonds frequent in aqueous solutions. Unlike other MLMD approaches that produce pairwise inter-atomic potentials,<sup>49,54,55</sup> our PDMD affords system energy and atomic forces directly from atomic coordinates and atom types, which are its sole input. This unique feature allows PDMD to capture the many-body effect efficaciously without being limited to the pairwise approximation, which breaks down in many aqueous systems due to the intrinsic non-addictive interactions within them.<sup>56</sup> Although explicitly learned three-body potentials can partially encode this critical many-bond effect as shown in a bcc tungsten crystal using cubic B-spline basis functions,<sup>57</sup> the broken symmetry in amorphous systems such as liquid water would make the potential energy surface too complicated for any predefined basis functions due to the complexity of geometric features. Our PDMD model can address this challenge well by employing multiple aggregators with self-adaptive weights to accurately encode an atom’s chemical environment for arbitrary atomic spatial patterns. As shown by our benchmark systems of  $(\text{H}_2\text{O})_{1 \leq n \leq 21}$  clusters, both gas-like and liquid-like molecular structures are satisfactorily delineated by PDMD, exhibiting remarkably small energy MAE of 7.1 meV/atom, which is nearly 100% better than its DeepMD counterpart (Fig. 4(a)). Similarly, in terms of force MAE, PDMD outperforms DeepMD by  $\sim 200\%$  and is on par with GNNFF. More importantly, the delicate topology of the hydrogen bond network is also

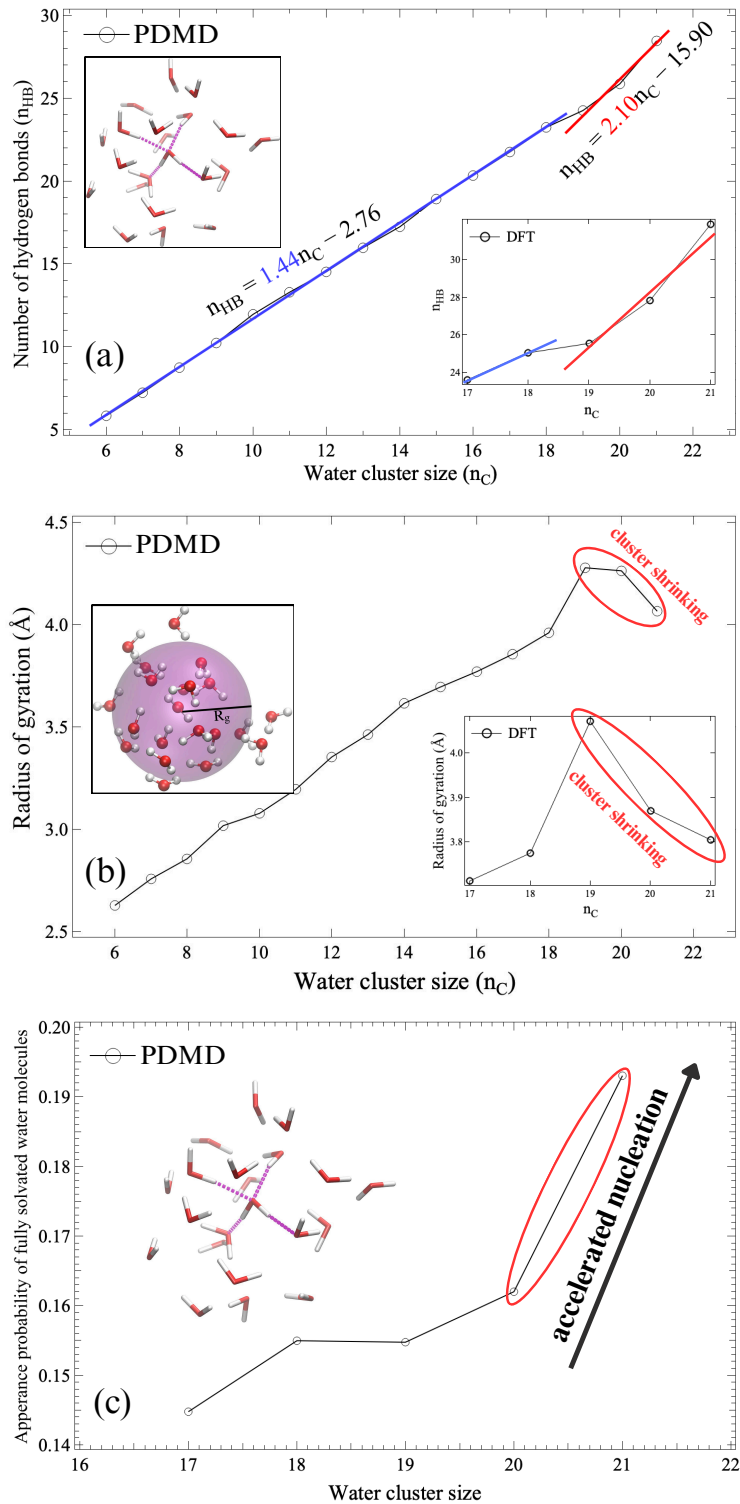


Figure 7: Dependence of (a) hydrogen bond number, (b) radius of gyration, and (c) appearance probability of fully solvated water molecules on water cluster size in long PDMD trajectories. For (a) and (b), the results extracted from short DFT/PBE trajectories are also shown in the insets.

precisely characterized by PDMD, leading to the consistent radius of gyration and the number of hydrogen bonds compared to AIMD for large water clusters ( $(\text{H}_2\text{O})_{6 \leq n \leq 21}$ ). For small water clusters ( $(\text{H}_2\text{O})_{1 \leq n \leq 5}$ ), their pseudo-planar optimized structures are well reproduced by PDMD. Most excitingly, PDMD also caught the abnormal cluster shrinking when the water cluster size approached 21, the experimentally observed magic number for the onset of the gas-liquid phase transition that can be ascribed to the accelerated nucleation with more fully solvated water molecules, each of which serves as the donor of two hydrogen bonds and the acceptor of two others.

Given the high fidelity and exceptional efficiency of PDMD, chemical reactions in some large systems can be explored. One of them is the proton transfer in aqueous solutions. The energy barrier for proton transfer in liquid water is known to be as small as  $\sim 1$  kcal/mol, which is approximately the energy difference between a solvated Eigen and a solvated Zundel cation.<sup>58</sup> More interestingly, the proton transfer proceeds through the Grotthuss mechanism, wherein a transferring proton is passed from one water molecule to another by breaking a hydrogen bond and forming another without the need for atomic displacement. This unique necessity of dynamic bonding topology invalidates the application of conventional empirical force fields with fixed chemical bonds. Therefore, proton transfer in aqueous solutions can be only treated by the computationally demanding AIMD or a slightly more cost-effective semi-empirical multi-state empirical valence bond (MS-EVB) theory,<sup>19</sup> which was parameterized to reproduce the quantum PES for protonated water dimer and tetramer. Nevertheless, MS-EVB's significantly underestimated proton diffusion coefficient<sup>19</sup> suggests an incomplete representation of the proton transfer reaction coordinate due to the missing solvation shell during its parameterization, which our data-driven PDMD can mitigate through a sufficient sampling of fully solvated protonated water molecules under arbitrary pH. In fact, PDMD would be especially useful for high-pH simulations, which demand a vast number of water molecules. Another system that will benefit from PDMD is aqueous solutions containing anions. Anions are typically polarizable due to their rather diffuse electronic wavefunctions,<sup>59</sup> making the many-body London dispersion interactions particularly prominent despite the strong screening effect in water. On that account, polarizable force fields<sup>5</sup> have to be adopted to account for the mutual polarization of anions through a self-consistent approach, which notably comprises its numerical advantages over AIMD. By contrast, our potential-free PDMD naturally encodes the many-body

interactions as much as is allowed by the statistical sampling of a chemical system with non-additive couplings, which are also critical in molecular solids<sup>60</sup> and biological systems.<sup>61</sup> To address these challenges, we plan to refine our PDMD model by leveraging hypergraphs to capture the many-body nature of dispersion forces. In this approach, a hyperedge would connect all atoms involved in a particular collective interaction, thereby more accurately reflecting the many-body correlations than a simple pairwise graph. In summary, PDMD outperforms the current state-of-the-art approaches in machine learning molecular dynamics by offering chemically adaptive aggregators and lays a solid foundation for future improvements through enhanced expressiveness and generalization of chemical hypergraphs,<sup>62</sup> particularly for chemical reactions.<sup>63</sup>

## Methods

### a. Generation of Machine Learning Datasets

The construction of our ML datasets resonates with an iterative self-consistent model training approach that will be delineated in Subsection (c). Unless otherwise specified, all *ab initio* calculations were performed by CP2K,<sup>64</sup> an open-source molecular simulation package, with the Goedecker–Teter–Hutter (GTH) pseudopotential,<sup>65</sup> Perdew–Burke–Ernzerhof (PBE) exchange–correlation functional,<sup>48</sup> polarized–valence–double- $\zeta$  (PVDZ) basis set,<sup>66</sup> and wavelet-based Poisson solver.<sup>67</sup> All initial structures of  $(\text{H}_2\text{O})_n$  were obtained from a DFT study<sup>52</sup> at the M06-2X/6-311++g(d,p) level of theory.<sup>68</sup> For each initial structure, an AIMD simulation at 300 K was carried out to afford a 1-ns long trajectory before some snapshots were randomly selected. Then, the  $E$  and  $\vec{F}_i$  of those chosen snapshots were evaluated to construct our ML dataset’s first subset, which entails 63,000  $(\text{H}_2\text{O})_n$  structures. After the first round of machine learning model training, the optimized PDMD model was employed to generate a 200-ns long MLMD trajectory at 300 K, from which 100,000 more snapshots were randomly extracted to expand our ML dataset after their  $E$  and  $\vec{F}_i$  had been evaluated. For each subsequent round, 20,000 additional snapshots were extracted in the same manner. The expansion of this dataset only ceased when the desired accuracy of  $E$  and  $\vec{F}_i$  was achieved for our PDMD model. In total, our ML database consists of around 270,000  $(\text{H}_2\text{O})_n$  structures.

## b. ChemGNN Model

The core of the ChemGNN model is the chemical environment adaptive learning (CEAL) convolutional layer (see Fig. 8), which is defined as the following.

$$\mathbf{h}_{i,A}^{(k)} = \bigoplus_{j \in N(i)} MLP_{msg}^{(k)}(\mathbf{x}_i^{(k-1)}, \mathbf{x}_j^{(k-1)}, \mathbf{e}_{ji}), A \in \{0, \dots, M-1\} \quad (1)$$

$$\mathbf{x}_i^{(k)} = MLP_{update}^{(k)}(\mathbf{x}_i^{(k-1)}, w_0^{(k)} \cdot \mathbf{h}_{i,0}^{(k)}, \dots, w_{M-1}^{(k)} \cdot \mathbf{h}_{i,M-1}^{(k)}) \quad (2)$$

In the given equations, the variables  $i$  and  $j$  represent the central node and its adjacent nodes, denoted as  $j \in N(i)$ , respectively.  $\mathbf{x}_i^{(k-1)}$  and  $\mathbf{x}_j^{(k-1)}$  denote the node embeddings at the  $(k-1)$ -th convolutional layer for nodes  $i$  and  $j$ .  $\mathbf{e}_{ji}$  represents the edge embedding between nodes  $j$  and  $i$ . Every node’s embedding undergoes transformation by  $MLP_{msg}^{(k)}$ , consequently producing its respective message. Subsequently, these messages from the neighborhood are aggregated using the aggregator  $\bigoplus_A$ , where  $M$  denotes the number of employed aggregators. In this work, we employ five aggregators: sum, mean, max, min, and standard deviation (std). In the model’s  $k$ -th CEAL convolutional layer, we utilize trainable weights, represented as  $\mathbf{w}_A^{(k)}$ , to assign different levels of significance to the aggregated message  $\mathbf{h}_{i,A}^{(k)}$ . These weighted aggregated messages,  $\mathbf{w}_A^{(k)} \cdot \mathbf{h}_{i,A}^{(k)}$ , at the  $k$ -th layer, along with the central node’s embedding from the previous  $(k-1)$ -th layer, are used to update the node’s embedding through  $MLP_{update}^{(k)}$ .

## c. PDMD Framework

The architecture of PDMD is illustrated in Fig. 8. It leverages the effective representations of atomic chemical environments and utilizes the ChemGNN model, which excels at adaptively capturing the features of local environmental information to predict the system’s energy and atomic forces. The input dataset comprises snapshots of  $(\text{H}_2\text{O})_{1 \leq n \leq 21}$  obtained from MD simulations, including some configurations at the onset of the gas-liquid phase transition. Each snapshot provides the atomic species  $Z_i$  and Cartesian coordinates of atoms  $\vec{X}_i$  as input. However, several challenges arise from the input representation. For example, the input’s atomic coordinates depend on absolute position and orientation. Therefore, the Smooth Overlap of Atomic Positions (SOAP) descriptor<sup>69,70</sup> is used to enforce equivalence across equivalent structures. Specifically,

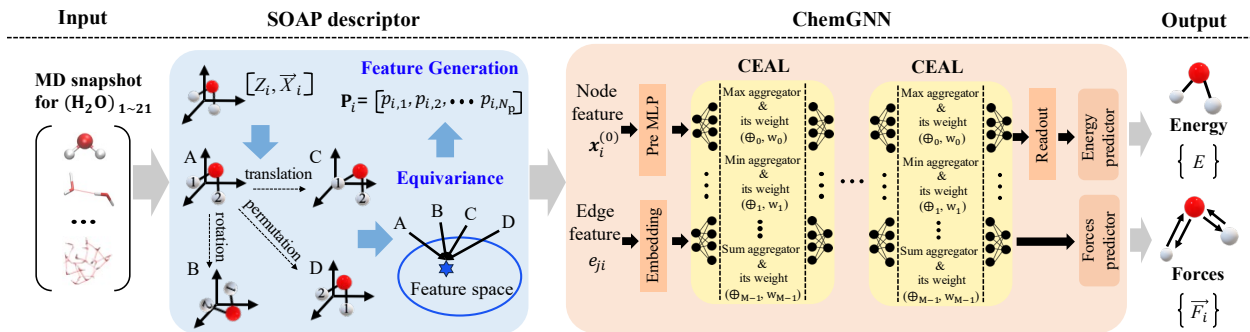


Figure 8: Overview of Potential-free Data-driven Molecular Dynamics (PDMD) for variable-sized water clusters  $(\text{H}_2\text{O})_n \leq 21$ .

SOAP utilizes orthogonal basis functions derived from spherical harmonics and radial basis functions to encode Gaussian-smearred atomic densities. By ensuring that all equivalent structures map to the same point in the feature space, SOAP further enriches the input atomic coordinates to invariant, higher-dimensional features, denoted as  $\mathbf{p}_i = [p_{i,1}, p_{i,2}, \dots, p_{i,N_p}]$ , where  $N_p$  represents the number of features for atom  $i$ .

Although the SOAP descriptor generates high-dimensional spatial representations, it does not include information about the atoms themselves. As a result, atom types are also incorporated as node features using a one-hot encoding vector,  $\mathbf{o}_i$ . Additionally, chemical bonds between atoms are represented as edges, with bond lengths serving as edge features. In our model, we utilized distinct cutoff distances to determine bonds: 1.6Å for H-H, 2.4Å for H-O, and 2.8Å for O-O. Each snapshot is thus represented as a graph  $G = (V, E, D)$ , where  $V$  is the set of atoms with initial node features  $\mathbf{x}_i^{(0)} = [\mathbf{o}_i, \mathbf{p}_i]$ .  $E$  represents the set of edges,  $D$  is the adjacency matrix that encodes the molecular topology, with  $D_{ji} = 1$  indicating an edge (chemical bond)  $e_{ji}$ , and  $D_{ji} = 0$  otherwise. This graph representation is then processed using the ChemGNN model. A pre-MLP and embedding layers are first applied to transform the node and edge features, enhancing their expressiveness. Next, the core CEAL layer of the ChemGNN model, equipped with an adaptive aggregation mechanism, is employed to fully extract essential information from various aspects of the nodes' chemical environments, thereby obtaining a high-level representation of the node. The model then splits into two pathways to predict the system's energy and atomic forces. In the first task, a readout layer performs pooling on the node embeddings to create a graph-level representation, which is passed through an Energy Predictor layer to predict the system energy  $E$ . In the second task, the node embeddings are directly fed



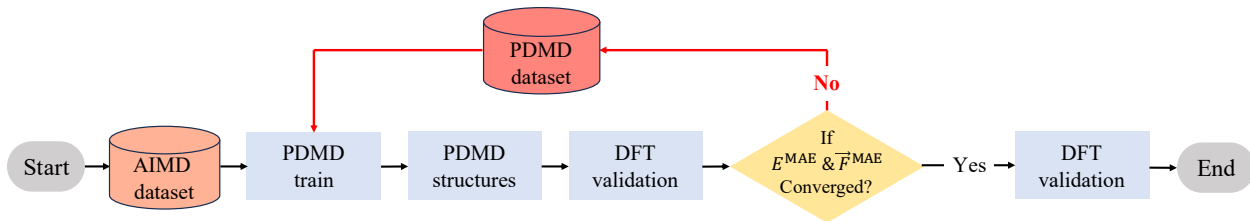


Figure 9: PDMD self-consistent model training cycle.

into a Force Predictor layer to predict force vectors for each atom,  $\vec{F}_i$ .

PDMD enables both node- and graph-level predictions, making MLMD simulations a practical tool for molecular dynamics. We can effortlessly generate numerous new structures through PDMD. Building on this capability, we employ an iterative process to expand the PDMD dataset by continuously generating and incorporating new snapshots, followed by retraining the model from scratch, as illustrated in Fig. 9. Initially, the AIMD dataset was the sole source for training the first version of the ML model. This model is then used for MD simulations to generate new snapshots for 200-ns, which are evaluated for model performance during this cycle. The newly generated PDMD data is added to the overall dataset for the subsequent training cycle. To determine model convergence, we monitor the difference in energy  $E^{\text{MAE}}$  and forces  $\vec{F}^{\text{MAE}}$  between cycle  $l$  and cycle  $l - 1$ . A convergence criterion is set, with energy and force differences limited to 1 meV/atom and 5 meV/Å, respectively. The iteration stops automatically and the converged ML model is saved when both  $\Delta E^{\text{MAE}} < 1$  meV/atom and  $\Delta \vec{F}^{\text{MAE}} < 5$  meV/Å. Our PDMD model achieved convergence after  $l = 4$  cycles.

#### d. Experimental Setup

We utilized two sets of hyperparameters to train the system energy and atomic forces prediction models, enabling PDMD to achieve near-optimal performance on both graph-level and node-level prediction tasks. The hyperparameters for optimizing both the energy and atomic force predictions are shown in Table. 1. The hyperparameters remained unchanged in each cycle of model training refined by the self-consistent method. All reported MAEs in this work are the average of three independent experiments.

PDMD demonstrates significant advantages in addressing the dual demands of accuracy and efficiency in molecular dynamics simulations. It achieves DFT-level accuracy in predicting system energy and atomic

<b>Hyperparameters</b>	<b>Energy Model</b>	<b>Force Model</b>
Initial learning rate	0.005	0.002
Minimum learning rate	$1 \times 10^{-6}$	$1 \times 10^{-7}$
Batch size	2048	1024
Epochs	3000	2000
CEAL layers	2	2
Optimizer	AdamW	Adam
Activation function	ReLU	ReLU
Scheduler mode	min	min
Factor	0.6	0.6
Patience	30	50

Table 1: Hyperparameter configurations for energy and force predictions of water clusters.

forces, significantly outperforming DeepMD, and possesses exceptional computational efficiency. Even for a small 10-water cluster, PDMD outperforms AIMD by a factor of 10,000 in terms of MD steps executed per day on a dual-socket 144-core NVIDIA Grace-Grace node equipped with Arm64 Noeverse V2 CPUs. Therefore, a much more significant performance gain, likely exceeding ten orders of magnitude, is expected for million-atom systems commonly seen in biomolecular research, further underscoring PDMD’s scalability and robustness. The iterative self-consistent approach allows continuous model refinement with each cycle to obtain the ideal model. Moreover, by combining SOAP descriptors and the ChemGNN model to handle variable-sized water clusters with multiple-phase coverage, PDMD effectively and adaptively captures the complexities of atomic chemical environments without a priori knowledge, making it a robust and scalable tool for ML-based molecular dynamics simulations.

## Data availability

Our dataset for  $(\text{H}_2\text{O})_{1 \leq n \leq 21}$  water clusters is freely available at [https://taccchen.s3.us-east-2.amazonaws.com/PDMD\\_DATASET/PDMD\\_DATASET.tar.gz](https://taccchen.s3.us-east-2.amazonaws.com/PDMD_DATASET/PDMD_DATASET.tar.gz).

## Code availability

Our PDMD code is freely available at <https://github.com/TACC/PDMD>.

## Acknowledgements

Computational resources were partially provided by the Texas Advanced Computing Center at the University of Texas at Austin.

## Competing interests

The authors declare no competing interests. All authors declare that they have no known competing financial interests or non-financial interests that could have appeared to influence the work reported in this paper.

## Author contributions

H. C., M. C., and Y. W. conceived and supervised the project. H. Y. and Q. D. implemented the models and performed the experiments. H. C., M. C., Y. W., and Q. D. performed the characterization and participated in the discussion. H. C., M. C., Y. W., and H. Y. wrote the original draft and created the visualizations. All authors read and agreed on the final version of the manuscript.

## References

- <sup>1</sup> Alder, B. J. & Wainwright, T. E. Studies in molecular dynamics. i. general method. *The Journal of Chemical Physics* **31**, 459–466 (1959).
- <sup>2</sup> Karplus, M. & McCammon, J. A. Molecular dynamics simulations of biomolecules. *Nature structural biology* **9**, 646–652 (2002).

- <sup>3</sup> Mouvet, F., Villard, J., Bolnykh, V. & Rothlisberger, U. Recent advances in first-principles based molecular dynamics. *Accounts of Chemical Research* **55**, 221–230 (2022).
- <sup>4</sup> Lifson, S. & Warshel, A. Consistent force field for calculations of conformations, vibrational spectra, and enthalpies of cycloalkane and n-alkane molecules. *The Journal of Chemical Physics* **49**, 5116–5129 (1968).
- <sup>5</sup> Warshel, A., Kato, M. & Pisliakov, A. V. Polarizable force fields: history, test cases, and prospects. *Journal of Chemical Theory and Computation* **3**, 2034–2045 (2007).
- <sup>6</sup> Iftimie, R., Minary, P. & Tuckerman, M. E. Ab initio molecular dynamics: Concepts, recent developments, and future trends. *Proceedings of the National Academy of Sciences* **102**, 6654–6659 (2005).
- <sup>7</sup> Schrödinger, E. An undulatory theory of the mechanics of atoms and molecules. *Physical review* **28**, 1049 (1926).
- <sup>8</sup> Feynman, R. P. Forces in molecules. *Physical review* **56**, 340 (1939).
- <sup>9</sup> Hohenberg, P. & Kohn, W. Inhomogeneous electron gas. *Physical review* **136**, B864 (1964).
- <sup>10</sup> Momany, F., McGuire, R. F., Burgess, A. & Scheraga, H. A. Energy parameters in polypeptides. vii. geometric parameters, partial atomic charges, nonbonded interactions, hydrogen bond interactions, and intrinsic torsional potentials for the naturally occurring amino acids. *The Journal of Physical Chemistry* **79**, 2361–2381 (1975).
- <sup>11</sup> Best, R. B. *et al.* Optimization of the additive charmm all-atom protein force field targeting improved sampling of the backbone  $\phi$ ,  $\psi$  and side-chain  $\chi_1$  and  $\chi_2$  dihedral angles. *Journal of chemical theory and computation* **8**, 3257–3273 (2012).

- <sup>12</sup> Tian, C. *et al.* ff19sb: amino-acid-specific protein backbone parameters trained against quantum mechanics energy surfaces in solution. *Journal of chemical theory and computation* **16**, 528–552 (2019).
- <sup>13</sup> Reif, M. M., Hünenberger, P. H. & Oostenbrink, C. New interaction parameters for charged amino acid side chains in the gromos force field. *Journal of chemical theory and computation* **8**, 3705–3723 (2012).
- <sup>14</sup> Harder, E. *et al.* Opls3: a force field providing broad coverage of drug-like small molecules and proteins. *Journal of chemical theory and computation* **12**, 281–296 (2016).
- <sup>15</sup> Shi, Y. *et al.* Polarizable atomic multipole-based amoeba force field for proteins. *Journal of chemical theory and computation* **9**, 4046–4063 (2013).
- <sup>16</sup> Huang, L. & Roux, B. Automated force field parameterization for nonpolarizable and polarizable atomic models based on ab initio target data. *Journal of chemical theory and computation* **9**, 3543–3556 (2013).
- <sup>17</sup> Fröhlking, T., Bernetti, M., Calonaci, N. & Bussi, G. Toward empirical force fields that match experimental observables. *The Journal of chemical physics* **152** (2020).
- <sup>18</sup> Senftle, T. P. *et al.* The reaxff reactive force-field: development, applications and future directions. *npj Computational Materials* **2**, 1–14 (2016).
- <sup>19</sup> Wu, Y., Chen, H., Wang, F., Paesani, F. & Voth, G. A. An improved multistate empirical valence bond model for aqueous proton solvation and transport. *The Journal of Physical Chemistry B* **112**, 467–482 (2008).
- <sup>20</sup> Turing, A. M. Computing machinery and intelligence. *Mind* **59**, 433–460 (1950). URL <http://www.jstor.org/stable/2251299>.

- <sup>21</sup> Noé, F., Tkatchenko, A., Müller, K.-R. & Clementi, C. Machine learning for molecular simulation. *Annual review of physical chemistry* **71**, 361–390 (2020).
- <sup>22</sup> Montáns, F. J., Chinesta, F., Gómez-Bombarelli, R. & Kutz, J. N. Data-driven modeling and learning in science and engineering. *Comptes Rendus Mécanique* **347**, 845–855 (2019).
- <sup>23</sup> Raghavachari, K. Electron correlation techniques in quantum chemistry: Recent advances. *Annual Review of Physical Chemistry* **42**, 615–642 (1991).
- <sup>24</sup> McMillan, W. L. Ground state of liquid he 4. *Physical Review* **138**, A442 (1965).
- <sup>25</sup> Ross, I. G. Calculations of the energy levels of acetylene by the method of antisymmetric molecular orbitals, including  $\sigma$ - $\pi$  interaction. *Transactions of the Faraday Society* **48**, 973–991 (1952).
- <sup>26</sup> Pfau, D., Spencer, J. S., Matthews, A. G. & Foulkes, W. M. C. Ab initio solution of the many-electron schrödinger equation with deep neural networks. *Physical review research* **2**, 033429 (2020).
- <sup>27</sup> Kochkov, D. *et al.* Machine learning–accelerated computational fluid dynamics. *Proceedings of the National Academy of Sciences* **118**, e2101784118 (2021).
- <sup>28</sup> Glowinski, R. & Pironneau, O. Finite element methods for navier-stokes equations. *Annual review of fluid mechanics* **24**, 167–204 (1992).
- <sup>29</sup> Li, Y. *et al.* Ai-assisted superresolution cosmological simulations. *Proceedings of the National Academy of Sciences* **118**, e2022038118 (2021).
- <sup>30</sup> Unke, O. T. *et al.* Machine learning force fields. *Chemical Reviews* **121**, 10142–10186 (2021).

- <sup>31</sup> Schölkopf, B., Smola, A. & Müller, K.-R. Nonlinear component analysis as a kernel eigenvalue problem. *Neural computation* **10**, 1299–1319 (1998).
- <sup>32</sup> Fukushima, K. Neocognitron: A self-organizing neural network model for a mechanism of pattern recognition unaffected by shift in position. *Biological cybernetics* **36**, 193–202 (1980).
- <sup>33</sup> Fukushima, K. Visual feature extraction by a multilayered network of analog threshold elements. *IEEE Transactions on Systems Science and Cybernetics* **5**, 322–333 (1969).
- <sup>34</sup> Morawietz, T., Singraber, A., Dellago, C. & Behler, J. How van der waals interactions determine the unique properties of water. *Proceedings of the National Academy of Sciences* **113**, 8368–8373 (2016).
- <sup>35</sup> Becke, A. D. Density-functional exchange-energy approximation with correct asymptotic behavior. *Physical review A* **38**, 3098 (1988).
- <sup>36</sup> Behler, J. Atom-centered symmetry functions for constructing high-dimensional neural network potentials. *The Journal of chemical physics* **134** (2011).
- <sup>37</sup> Smith, J. S., Isayev, O. & Roitberg, A. E. Ani-1: an extensible neural network potential with dft accuracy at force field computational cost. *Chemical science* **8**, 3192–3203 (2017).
- <sup>38</sup> Schütt, K. *et al.* Schnet: A continuous-filter convolutional neural network for modeling quantum interactions. *Advances in neural information processing systems* **30** (2017).
- <sup>39</sup> Scarselli, F., Gori, M., Tsoi, A. C., Hagenbuchner, M. & Monfardini, G. The graph neural network model. *IEEE transactions on neural networks* **20**, 61–80 (2008).

- <sup>40</sup> Hasebe, T. Knowledge-embedded message-passing neural networks: improving molecular property prediction with human knowledge. *ACS omega* **6**, 27955–27967 (2021).
- <sup>41</sup> Park, C. W. *et al.* Accurate and scalable graph neural network force field and molecular dynamics with direct force architecture. *npj Computational Materials* **7**, 73 (2021).
- <sup>42</sup> Choudhary, K. *et al.* Unified graph neural network force-field for the periodic table: solid state applications. *Digital Discovery* **2**, 346–355 (2023).
- <sup>43</sup> Chen, C. *et al.* Chemical environment adaptive learning for optical band gap prediction of doped graphitic carbon nitride nanosheets. *arXiv preprint arXiv:2302.09539* (2023).
- <sup>44</sup> Keutsch, F. N. & Saykally, R. J. Water clusters: Untangling the mysteries of the liquid, one molecule at a time. *Proceedings of the National Academy of Sciences* **98**, 10533–10540 (2001).
- <sup>45</sup> Rognoni, A., Conte, R. & Ceotto, M. How many water molecules are needed to solvate one? *Chemical Science* **12**, 2060–2064 (2021).
- <sup>46</sup> Brubach, J.-B., Mermet, A., Filabozzi, A., Gerschel, A. & Roy, P. Signatures of the hydrogen bonding in the infrared bands of water. *The Journal of chemical physics* **122** (2005).
- <sup>47</sup> Lee, C., Yang, W. & Parr, R. G. Development of the colle-salvetti correlation-energy formula into a functional of the electron density. *Physical review B* **37**, 785 (1988).
- <sup>48</sup> Perdew, J. P., Burke, K. & Ernzerhof, M. Generalized gradient approximation made simple. *Physical review letters* **77**, 3865 (1996).



- <sup>49</sup> Zeng, J. *et al.* Deepmd-kit v2: A software package for deep potential models. *The Journal of Chemical Physics* **159** (2023).
- <sup>50</sup> Wang, Y., Babin, V., Bowman, J. M. & Paesani, F. The water hexamer: cage, prism, or both. full dimensional quantum simulations say both. *Journal of the American Chemical Society* **134**, 11116–11119 (2012).
- <sup>51</sup> Latimer, W. M. & Rodebush, W. H. Polarity and ionization from the standpoint of the lewis theory of valence. *Journal of the American Chemical Society* **42**, 1419–1433 (1920).
- <sup>52</sup> Malloum, A., Fifen, J. J., Dhaouadi, Z., Engo, S. G. N. & Conradie, J. Structures, relative stability and binding energies of neutral water clusters,(h 2 o) 2–30. *New Journal of Chemistry* **43**, 13020–13037 (2019).
- <sup>53</sup> Silverstein, K. A., Haymet, A. & Dill, K. A. The strength of hydrogen bonds in liquid water and around nonpolar solutes. *Journal of the American Chemical Society* **122**, 8037–8041 (2000).
- <sup>54</sup> Musaelian, A. *et al.* Learning local equivariant representations for large-scale atomistic dynamics. *Nature Communications* **14**, 579 (2023).
- <sup>55</sup> Wang, W., Wu, Z., Dietschreit, J. C. & Gómez-Bombarelli, R. Learning pair potentials using differentiable simulations. *The Journal of Chemical Physics* **158** (2023).
- <sup>56</sup> Herman, K. M., Stone, A. J. & Xantheas, S. S. A classical model for three-body interactions in aqueous ionic systems. *The Journal of Chemical Physics* **157** (2022).
- <sup>57</sup> Xie, S. R., Rupp, M. & Hennig, R. G. Ultra-fast interpretable machine-learning potentials. *npj Computational Materials* **9**, 162 (2023).

- <sup>58</sup> Swanson, J. M. *et al.* Proton solvation and transport in aqueous and biomolecular systems: Insights from computer simulations. *The Journal of Physical Chemistry B* **111**, 4300–4314 (2007).
- <sup>59</sup> Simons, J. Molecular anions. *The Journal of Physical Chemistry A* **112**, 6401–6511 (2008).
- <sup>60</sup> Jansen, L. Systematic analysis of many-body interactions in molecular solids. *Physical Review* **125**, 1798 (1962).
- <sup>61</sup> Ejtehadi, M., Avall, S. & Plotkin, S. Three-body interactions improve the prediction of rate and mechanism in protein folding models. *Proceedings of the National Academy of Sciences* **101**, 15088–15093 (2004).
- <sup>62</sup> Konstantinova, E. V. & Skorobogatov, V. A. Application of hypergraph theory in chemistry. *Discrete Mathematics* **235**, 365–383 (2001).
- <sup>63</sup> Jost, J. & Mulas, R. Hypergraph laplace operators for chemical reaction networks. *Advances in mathematics* **351**, 870–896 (2019).
- <sup>64</sup> Kühne, T. D. *et al.* Cp2k: An electronic structure and molecular dynamics software package-quickstep: Efficient and accurate electronic structure calculations. *The Journal of Chemical Physics* **152** (2020).
- <sup>65</sup> Goedecker, S., Teter, M. & Hutter, J. Separable dual-space gaussian pseudopotentials. *Physical Review B* **54**, 1703 (1996).
- <sup>66</sup> Woon, D. E. & Dunning Jr, T. H. Gaussian basis sets for use in correlated molecular calculations. iv. calculation of static electrical response properties. *The Journal of chemical physics* **100**, 2975–2988 (1994).

- <sup>67</sup> Genovese, L., Deutsch, T., Neelov, A., Goedecker, S. & Beylkin, G. Efficient solution of poisson's equation with free boundary conditions. *The Journal of chemical physics* **125** (2006).
- <sup>68</sup> Zhao, Y. & Truhlar, D. G. The m06 suite of density functionals for main group thermochemistry, thermochemical kinetics, noncovalent interactions, excited states, and transition elements: two new functionals and systematic testing of four m06-class functionals and 12 other functionals. *Theoretical chemistry accounts* **120**, 215–241 (2008).
- <sup>69</sup> De, S., Bartók, A. P., Csányi, G. & Ceriotti, M. Comparing molecules and solids across structural and alchemical space. *Physical Chemistry Chemical Physics* **18**, 13754–13769 (2016).
- <sup>70</sup> Laakso, J. *et al.* Updates to the dscribe library: New descriptors and derivatives. *The Journal of Chemical Physics* **158** (2023).